Supporting Information

Understanding Piezoelectricity of High-Performance Potassium Sodium Niobate Ceramics from Diffused Multi-phase Coexistence and Domain Feature

Xi-xi Sun[1,+], Junwei Zhang[2,+], Xiang Lv[1*], Xi-xiang Zhang[2*], Yao Liu[3], Fei Li[3], and Jiagang Wu[1*]

[1]Department of Materials Science, Sichuan University, Chengdu, 610065, P. R. China

[2]Division of Physical Science and Engineering (PSE), King Abdullah University of Science and Technology (KAUST), Thuwal, 23955-6900, Saudi Arabia

[3]Electronic Materials Research Laboratory, Key Laboratory of the Ministry of Education, Xi'an Jiaotong University, Xi'an, 710049, P. R. China

*Correspondence e-mail: wujiagang0208@163.com and msewujg@scu.edu.cn (J. Wu), lvxiangscu@163.com (X, Lv), and xixiang.zhang@kaust.edu.sa (X. Zhang)

[+]Xi-xi Sun and Junwei Zhang contributed equally to this work.

1. Experimental procedure

***Composition design*:** The previous publications proved that the multi-phase coexistence is the most effective way to improve the piezoelectric properties of KNN-based and other piezoceramics [1]. To obtain the multi-phase coexistence in KNN-based ceramics, the addition of some additives is indispensable [1]. Our previous review has systematically summarized the possible additives that could effectively shift the phase transition temperatures (i.e., rhombohedral-orthorhombic phase transition temperature ($T_{R\text{-}O}$) and orthorhombic-tetragonal phase transition temperature ($T_{O\text{-}T}$) of KNN ceramics [1]. The conclusions showed that Sb^{5+} and $AZrO_3$ [A=Ca, Sr, Ba or $(Bi_{0.5}Ag_{0.5})$, and $(Bi_{0.5}Na_{0.5})$] can effectively tailor $T_{R\text{-}O}$ and $T_{O\text{-}T}$ of KNN ceramics. For example, the addition of $(Bi_{0.5}Ag_{0.5})ZrO_3$ simultaneously shifted $T_{R\text{-}O}$ and $T_{O\text{-}T}$ of KNNS ceramics to room temperature, resulting in a multi-phase coexistence in KNNS-BAZ ceramics [2]. $SrZrO_3$ was also reported to reduce $T_{O\text{-}T}$ of KNLNS ceramics [3], while Sb^{5+} could quickly increase $T_{R\text{-}O}$ of KNN ceramics [4]. Therefore, we chose $(0.99\text{-}x)(K_{0.48}Na_{0.52})(Nb_{0.955}Sb_{0.045})O_3\text{-}0.01SrZrO_3\text{-}x(Bi_{0.5}Ag_{0.5})ZrO_3$ as an example to obtain the room-temperature multi-phase coexistence and unveil the related physical mechanisms of the enhanced piezoelectric properties.

***Preparation of materials*:** $(0.99\text{-}x)(K_{0.48}Na_{0.52})(Nb_{0.955}Sb_{0.045})O_3\text{-}0.01SrZrO_3\text{-}x(Bi_{0.5}Ag_{0.5})ZrO_3$ (KNNS-SZ-BAZ, x=0-0.05) ceramics were fabricated by the solid-state method. K_2CO_3 (99%), Na_2CO_3 (99.8%), Nb_2O_5 (99.5%), Bi_2O_3 (99.999%), Sb_2O_3 (99.99%), $SrCO_3$ (99.9%), Ag_2O (99.7%) and ZrO_2 (99.5%) (Sinopharm Chemical Reagent Co., Ltd, China) were selected as raw materials. All raw materials were dried

at 180 °C for 3 h due to the hygroscopicity. Mixtures of the raw materials with the designed compositions were ball-milled for 24 h with zirconia ball media and alcohol in plastic jars. Then, the dried slurry was calcined at 850 °C for 6 h. The calcined powder was pressed into disks of 10 mm diameter and 1 mm thickness under 10 MPa using PVA as a binder. After burning off the PVA at 500 °C, the disks were sintered at 1060-1120 °C for 3 h under a corundum crucible in air. To characterize the electric properties of the materials, silver paste was printed on both sides of the as-sintered disks, which were then baked at 600 °C for 30 min to form electrodes. The piezoelectric properties were measured by poling the samples with a DC electric field of 40 kV/cm for 30 min in a silicone oil bath at room temperature.

***Characterization*:** The crystal information was collected by X-ray diffraction (XRD) (Bruker D8 Advance XRD, BrukerAXS Inc., Madison, WI, Cu-K_{α}). The as-sintered samples with x=0.03 were ground into powder and then annealed at 600 °C for 30 min to eliminate internal stress. The powder XRD data was collected using a high-resolution XRD apparatus (X' Pert Pro MPD, DY 120 PANalytical, Netherlands). Maud software package was used to conduct the Rietveld refinement. *in situ* temperature-dependent Raman spectra in the range of 100-1000 cm^{-1} were measured by a Raman equipment (Horiba Aramis, Horiba Scientific, Japan) with the excitation source of 473 nm radiation, in connection with external temperature controller (HFS600E-PB4/PB2, Linkam Scientific Instruments, UK). The samples for transmission electron microscopy (TEM) were prepared by focused ion beam (FIB, Helios G4, Thermo Fisher Scientific, USA). The domain structures were collected by a FEI Titan 80-300 electron microscope (Thermo Fisher Scientific, USA) with an accelerating voltage of 300 kV. To perform the measurement of piezoresponse force microscopy (PFM), the as-sintered samples

were polished by hand, using the diamond polishing slurry with different particle sizes as polishing media. The PFM observations were conducted on a commercial atomic force microscope (MFP-3D, Asylum Research, Goleta, CA) with a conductive Pt-Ir-coated cantilever PPP-NCHPt (Nanosensors, Switzerland).

The direct piezoelectric coefficient (d_{33}) of the poled samples was measured by a quasi-static d_{33} meter (ZJ-3 A, China) after aging for 24 hours. Temperature-dependent dielectric properties (e.g., relative permittivity ε_r, real part of permittivity ε', imaginary part of permittivity ε'', and dielectric loss tan δ) were measured by a broadband dielectric spectrometer (Novocontrol Concept 80, Novocontrol, German). The room-temperature dielectric properties (e.g., ε_r and tan δ) were measured by a LCR analyzer (HP 4980, Agilent, USA). The polarization-electric field (*P*-*E*) loops were measured via a ferroelectric analyzer (aixACCT TF Analyzer 2000, Germany), at a frequency of 1 Hz.

***Phenomenological theory*:** Based on Landau-Ginsburg-Devonshire phenomenological model, the density of Gibbs free energy for stress-free ferroelectric can be expressed as [5]:

$$\Delta G = \alpha_1\left(P_1^2+P_2^2+P_3^2\right)+\alpha_{11}\left(P_1^4+P_2^4+P_3^4\right)+\alpha_{12}\left(P_1^2P_2^2+P_1^2P_3^2+P_2^2P_3^2\right)+\alpha_{112}\left[P_1^4\left(P_2^2+P_3^2\right)\right.$$
$$\left.+P_2^4\left(P_1^2+P_3^2\right)+P_3^4\left(P_1^2+P_2^2\right)\right]+\alpha_{111}\left(P_1^6+P_2^6+P_3^6\right)+\alpha_{123}P_1^2P_2^2P_3^2-E_1P_1-E_2P_2-E_3P_3$$

where P_i (i=1, 2, 3) is the polarization, E_i (i=1, 2, 3) the corresponding applied external electric-field. α_1, α_{11}, α_{12}, α_{111}, α_{112} and α_{123} are Landau energy coefficients, whose values determine the thermodynamic behavior of ferroelectric phases, ferroelectric

transition temperature and the stability of ferroelectric phases. According to dielectric properties and phase transition temperature of $0.955K_{0.48}Na_{0.52}Nb_{0.955}Sb_{0.045}O_3$-$0.01SrZrO_3$-$0.035(Bi_{0.5}Ag_{0.5})ZrO_3$, the Landau coefficients are set to be:

$\alpha_1 = 2.273\times10^6$*(tem-498) $C^{-2}m^2N$,

$\alpha_{11} = 2.647\times10^6$*(tem-508) $C^{-4}m^6N$,

$\alpha_{12} = 9.66\times10^8$ $C^{-4}m^6N$,

$\alpha_{111} = (-5.86\times10^7$(tem-508)$-2.81\times10^9)$ $C^{-6}m^{10}N$,

$\alpha_{112} = -1.99\times10^9$ $C^{-6}m^{10}N$,

$\alpha_{123} = 1.55\times10^{10}$ $C^{-6}m^{10}N$.

2. Supporting Materials

Fig. S1(a) shows the XRD patterns of KNNS-SZ-BAZ ceramics as a function of *x*. All compositions exhibited a typical perovskite structure without detectable secondary phases, indicating that all additives have effectively diffused into KNN ceramics' lattice. Then, $\{200\}_{pc}$ peaks were amplified to further show the variations of phase structure, as shown in Fig. S1(b). With increasing *x*, $\{200\}_{pc}$ peaks gradually shifted to lower θ, indicating the expansion of interplanar spacing. The shifting of XRD patterns was due to the difference of ion radius of Nb^{5+} with Zr^{4+} (CN=6, $R_{Nb^{5+}}$=0.64 Å, $R_{Zr^{4+}}$=0.72 Å) [6]. Therefore, the substitution of Nb^{5+} with Zr^{4+} will slightly expand the interplanar spacing, resulting in the shifting of XRD patterns to lower θ [7,8]. For the ceramics with *x*=0, the intensity of $(002)_{pc}$ (I_{002}) was as twice high as that of $(200)_{pc}$ (I_{200}), indicating an orthorhombic (O) phase [9]. With an increase of *x*, I_{002} decreased while I_{200} increased, suggesting the involvement of tetragonal (T) phase. In the composition range of *x*=0.025-0.03, $(002)_{pc}$ and $(200)_{pc}$ exhibited the comparable intensity, indicating an O-T phase boundary [9]. As *x* increased up to 0.035, I_{200} was much higher than I_{002}, which was previously treated as the symbol of O-T, R-O-T or R-T phase coexistence [3,10]. When *x* further reached to 0.04 and 0.05, $\{200\}_{pc}$ gradually changed into a single peak, indicating the occurrence of cubic (C) or pseudo-cubic (PC) phase [11].

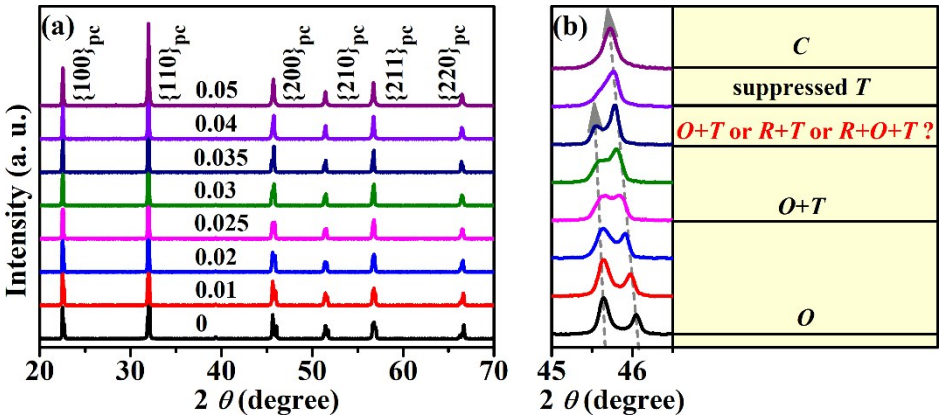

Figure S1. XRD patterns of unpoled KNNS-SZ-BAZ ceramics with 2θ=20-70° (a) and 45-46° (b).

To further judge the variations of phase structure, ε'-T, ε''-T, and tan δ-T curves of unpoled KNNS-SZ-BAZ ceramics were measured, as shown in Figs. S2(a-c). ε'-T curves showed that the orthorhombic-tetragonal phase transition temperature ($T_{O\text{-}T}$) of KNNS-SZ-BAZ ceramics gradually reduced at x=0-0.035 and decreased to room temperature at x=0.035. The ceramics with x=0.04 exhibited the seriously suppressed $T_{O\text{-}T}$, while no distinct $T_{O\text{-}T}$ was observed in the ceramics with x=0.05. The rhombohedral-orthorhombic phase transition temperature ($T_{R\text{-}O}$) can be observed indistinctly at x=0-0.025, and then disappeared at $x\geq$0.03. ε''-T curves showed that $T_{O\text{-}T}$ monotonously reduced with increasing x, while $T_{R\text{-}O}$ first increased and then became diffused, resulting the convergence of $T_{O\text{-}T}$ and $T_{R\text{-}O}$ (e.g., $T_{R\text{-}O\&O\text{-}T}$) at $x\geq$0.03. Thus, the ceramics with x=0.035 exhibited a $T_{R\text{-}O\&O\text{-}T}$ of 9.3 °C close to room temperature, indicating a R-O-T phase coexistence at room temperature. While the ceramics with x=0.05 only exhibited a Curie temperature (T_c) of 7 °C, manifesting a cubic (C) phase at room temperature. The similar diffusion or depression of $T_{R\text{-}O}$ was also observed in

other KNN-based ceramics [3]. Therefore, the addition of $(Bi_{0.5}Ag_{0.5})ZrO_3$ simultaneously decreased $T_{O\text{-}T}$ and made $T_{R\text{-}O}$ diffused. Interestingly, it was noted that ε'-T curves exhibited the higher $T_{O\text{-}T}$ values than those in ε''-T curves, and the difference was improved with increasing x, indicating the increased degree of diffuseness.

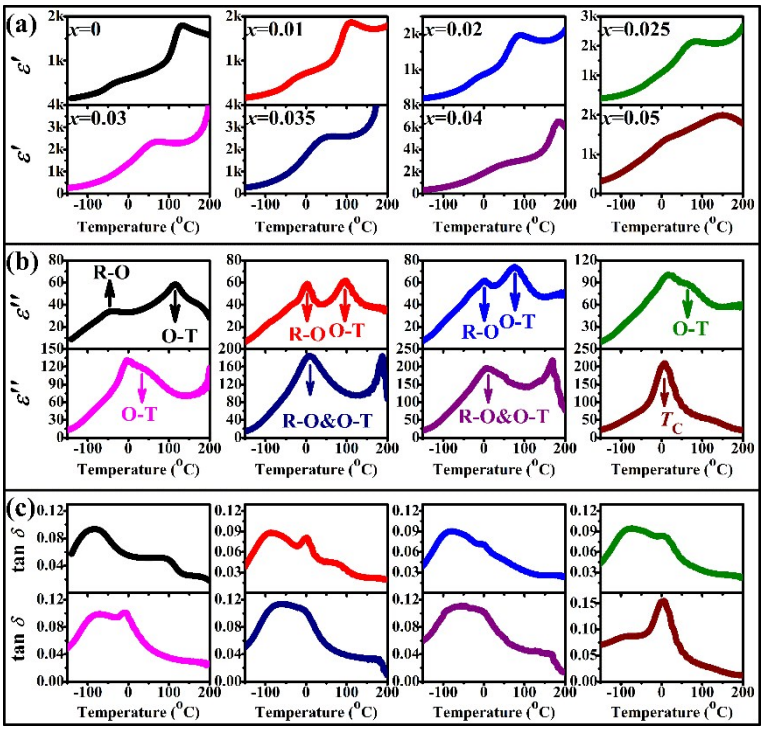

Figure S2. (a) ε', (b) ε'', and (c) tan δ of unpoled KNNS-SZ-BAZ ceramics, measured at 100 kHz.

To further identify the phase structure of the unpoled ceramics with x=0.035, the careful Rietveld refinement was conducted on the unpoled ceramics with x=0.035 using different combinations (e.g., O+T, R+T, R-O-T), as shown in Figure S3. The matching degree of these combinations was R-O-T>O-T>R+T, as proved by R_w and Sig values in Figs. S3(a1, b1, c1). However, it was also worth noting that the O+T combination exhibited the R_w and Sig values close to those of the R+O+T combination, indicating

the ceramics mainly possessed an O+T phase coexistence. The obtained phase proportion of R-O-T coexistence phase also supported this hypothesis, in which a low content for R phase while high content for O and T phase (see Table S2). In addition, the misfit regions were also marked by the green arrows. Obviously, the refinement using R+T combination exhibited the substantial discrepancies, while the ones using R+O+T and O+T combinations possessed a few of discrepancies. Therefore, the Rietveld refinement proved that the unpoled ceramics with x=0.035 possessed a R-O-T phase coexistence. The detailed results of Rietveld refinement were listed in Table S2.

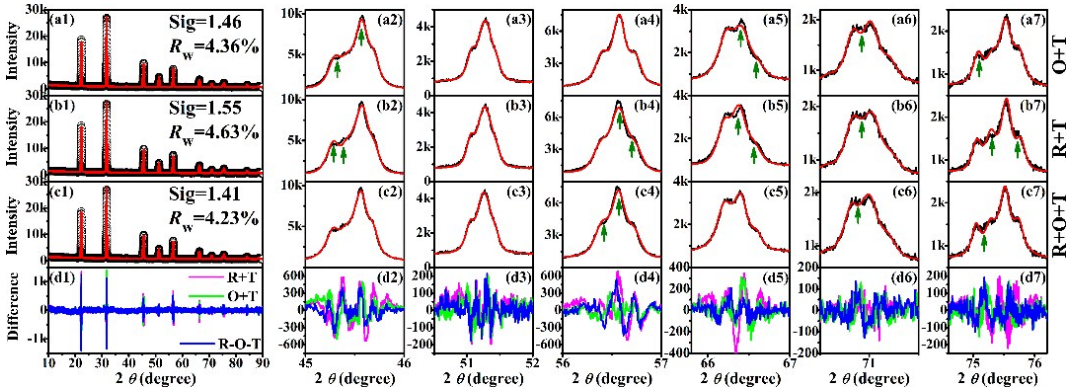

Figure S3. Rietveld refinement for the unpoled ceramic powder with x=0.035 using O+T (a1-a7), R+T (b1-b7), and R+O+T (c1-c7). (d1-d7) Difference of Rietveld refinements. The green arrows indicated the misfit regions.

Fig. S4(a) shows the ε'-T curves of unpoled KNNS-SZ-BAZ ceramics in the temperature range of 0-400 °C. Increasing x shifted the Curie temperature (T_c) to a lower temperature monotonously, as indicated by the arrow. Except for the reduction of T_c, the abnormal dielectric peak of T_c became broadened, indicating the increasing degree

of diffuseness. Here, the modified Curie-Weiss law was used to evaluate the diffuseness degree (γ) of unpoled KNNS-SZ-BAZ ceramics.

$$\frac{1}{\varepsilon(T)} - \frac{1}{\varepsilon_m} = \frac{(T - T_m)^\gamma}{C}$$

Where ε_m is the maximum permittivity at T_m, and C is the Curie-like constant. Classical ferroelectric exhibits a γ of 1, while a γ of 2 is for typical relaxor [12]. The unpoled ceramics with x=0.035 exhibited a more obvious deviation from Curie-Weiss law than that of the unpoled ceramics with x=0, indicating the increasing γ (Figs. S4(b) and (c)). Then, the linear fitting between ln(T-T_m) and ln ($1/\varepsilon'$-$1/\varepsilon_m'$) was conducted, whose slope represented the value of γ (Figs. S4(d) and (e)). Fig. S4(f) shows the variation of γ. As x increased from 0 to 0.05, γ increased monotonously from 1.32 to 1.99, resulting in a γ value of 1.53-1.57 in the compositions with nominal O-T or R-O-T phase coexistence (i.e., x=0.025-0.035). The increase of γ was mainly attributed to the increasing content of $(Bi_{0.5}Ag_{0.5})ZrO_3$ that will generate the local inhomogeneity (e.g., polar nanoregions, PNRs) [9]. Therefore, the unpoled ceramics with x=0.035 possessed a R-O-T phase coexistence with PNRs inclusions. Furthermore, the PNRs was highly suspected to be related with R phase due to the diffused $T_{R\text{-}O}$.

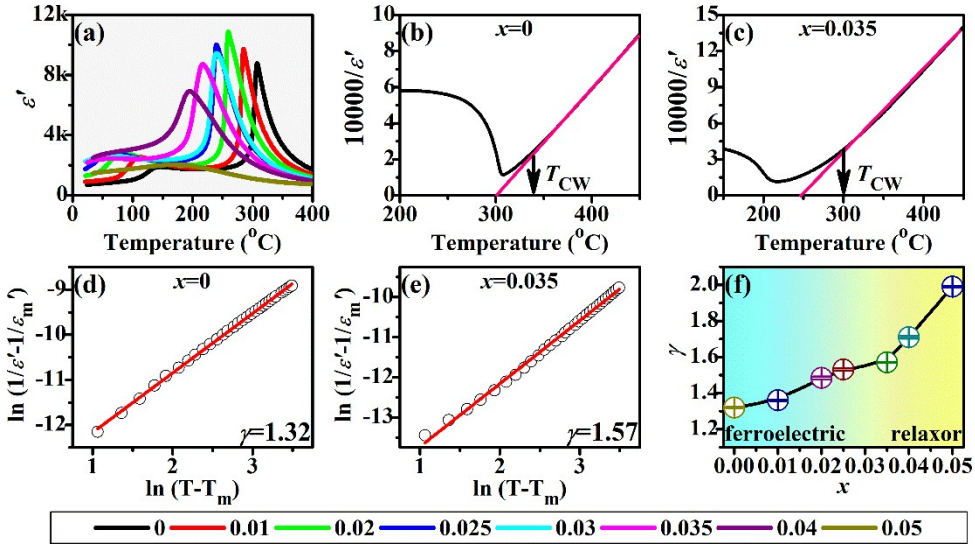

Figure S4. (a) ε'-T curves of unpoled KNNS-SZ-BAZ ceramics, measured at 100 kHz. Relationship of 1000/ε' and temperature of the unpoled ceramics with x=0 (b) and x=0.035 (c), measured at 100 kHz. Fitting of ln(T-T_m) *vs*. ln (1/ε'-1/ε'_m) for the unpoled ceramics with x=0 (d) and x=0.035 (e). Diffuseness degree (γ) of unpoled KNNS-SZ-BAZ ceramics as a function of x.

Figure S5 shows the temperature-dependent dielectric properties of poled KNNS-SZ-BAZ ceramics. ε'-T curves showed that the poled KNNS-SZ-BAZ ceramics exhibited the similar variations of $T_{O\text{-}T}$ to that of unpoled ones (Fig. S2(a)). While the almost unchanged $T_{R\text{-}O}$ (~-40 °C) can be distinctly observed at x=0-0.03 after poling. For the poled ceramics with x=0.035, $T_{R\text{-}O}$ became slightly diffused because $T_{O\text{-}T}$ reduced to 12.5 °C that was below room temperature. Therefore, the poled ceramics with x=0.035 should possess a nominal O-T phase coexistence at room temperature. While the poled ceramics with x=0.0.4 exhibited the completely converged $T_{R\text{-}O}$ and $T_{O\text{-}T}$ at 0 °C, suggesting a T phase at room temperature. Finally, the ceramics with x=0.05 only exhibited one abnormal peak at 25 °C, which corresponded to T_c, indicating a C phase

at room temperature. Therefore, the poling process reinforced the R phase, resulting in the separated $T_{R\text{-}O}$ and $T_{O\text{-}T}$ in the composition range of x=0-0.035.

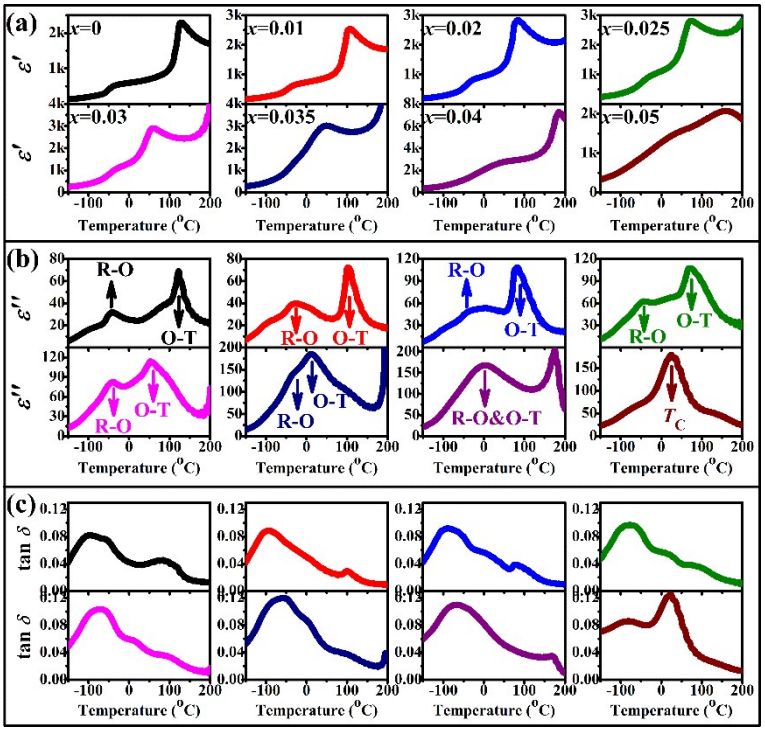

Figure S5. (a) ε', (b) ε'', and (c) tan δ of poled KNNS-SZ-BAZ ceramics varying with temperature, measured at 100 kHz.

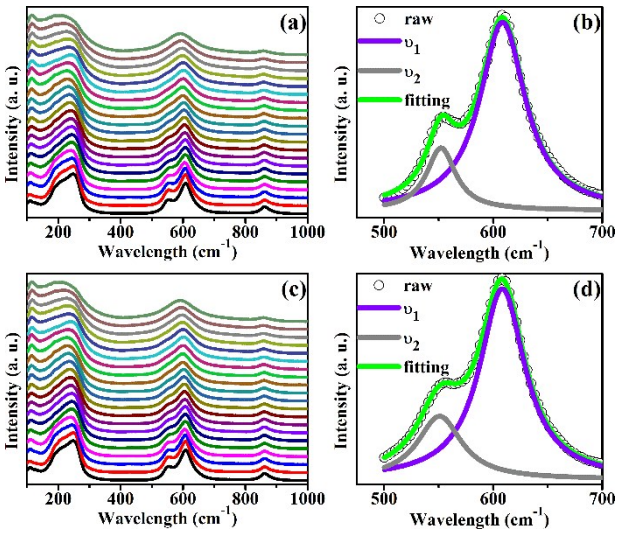

Figure S6. Temperature-dependent Raman spectra and Lorentz fitting for Raman spectrum at T=-150 °C of unpoled ceramics with x=0 (a, b) and x=0.035 (c, d).

Figures S7 (a) and (d) show the unpoled and poled ε'-T curves of the ceramics with x=0 and x=0.035. The increased ε' was observed at phase transition temperatures after poling, as marked by the arrows. In addition, γ of the poled ceramics with x=0 reduced to 1.19, while the poled ceramics with x=0.035 still exhibited a γ as high as 1.52.

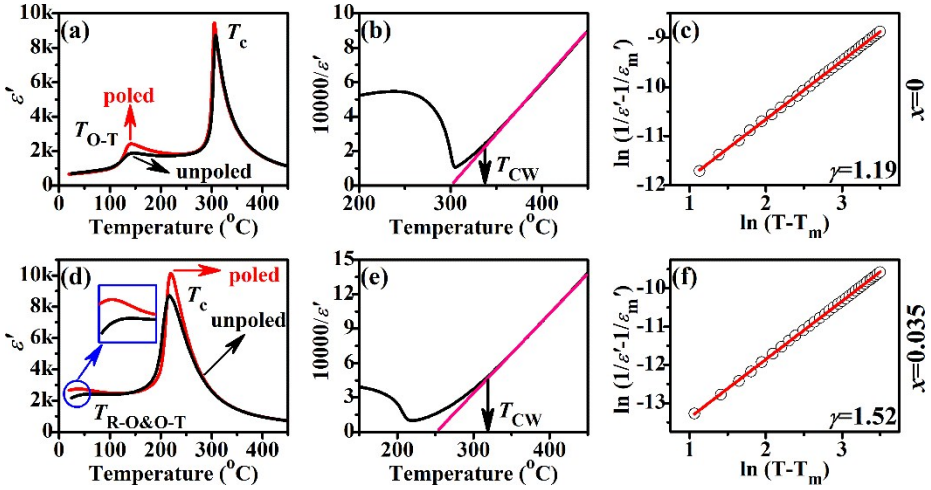

Figure S7. ε'-T curves of unpoled and poled ceramics with x=0 (a) and x=0.035 (d), measured at 100 kHz. 1000/ε'-T curve and linear fitting of ln(T-T_m) *vs*. ln (1/ε'-1/ε_m') for the poled ceramics with x=0 (b, c) and x=0.035 (e, f).

Figures S8 (a) and (b) show the distributions of domain structure in the case of single and multi-domain configurations. When one deliberately cut the domain zone into areas with different thicknesses, the obvious stairs will be formed (Figs. S8(a) and (b)). When crossing the stairs, the similar and continuous distribution will still be observed in a single domain zone, but not be found in a multi-domain zone (Figs. S8(a) and (b)), whereby the two domain structures can be distinguished.

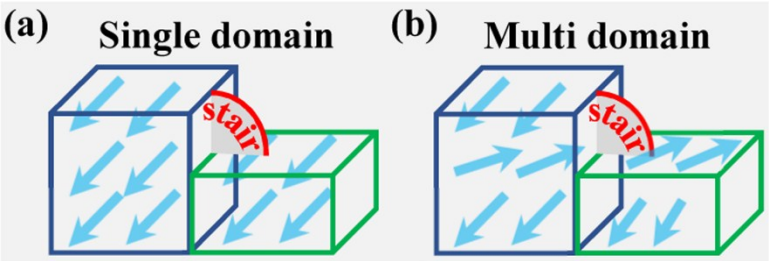

Figure S8. Schematic diagram of (a) single and (b) multi domains with different thicknesses.

In addition to the variations of γ, the phase angle was also measured to reflect the degree of saturation after poling, as shown in Figure S9. For an ideal poling, a phase degree of 90° is expected [13]. After poling, the ceramics with x=0 exhibited a phase degree of 74° while the ones with x=0.035 displayed a lower phase degree of 58°. Therefore, the poled ceramics with x=0.035 still exhibited the high disordered (diffuseness) degree, while the poled ceramics with x=0 showed the high ordered (low diffuseness) degree.

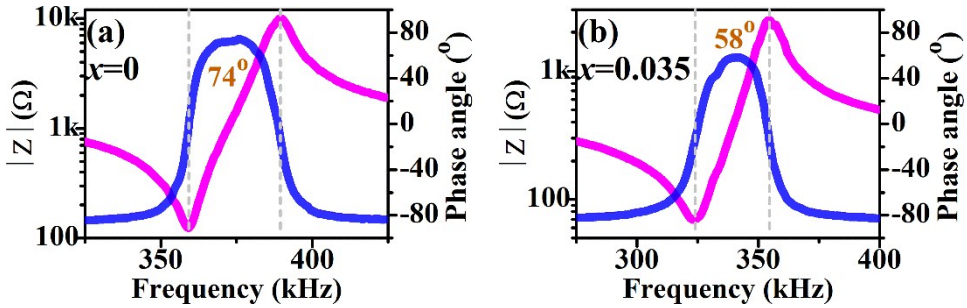

Figure S9. Frequency dependence of impedance |Z| and phase angle (°) for resonance measurements in poled ceramics with x=0 (a) and x=0.035 (b).

To further reveal the insufficient poling process, Raman spectra of the ceramics with x=0 and x=0.035 were collected before and after poling, as shown in Figures S10-S11. v_1 mode, which represents a double degenerate symmetric O-Nb-O stretching vibration,

was used to reflect the distance of Nb-O bond [14]. To exclude the accidental error, three or five points in different areas were used to collect Raman spectra. After poling, the position of v_1 shifted to lower wavelength, indicating the reduction of bond energy induced by the increasing Nb-O bond length [14]. Importantly, the ceramics with x=0 exhibited a reduction of 3~4.5 cm^{-1}, while a lower reduction of 1.5~2.5 cm^{-1} was found in the ones with x=0.035, indicating the more sufficient poling process in the ceramics with x=0.

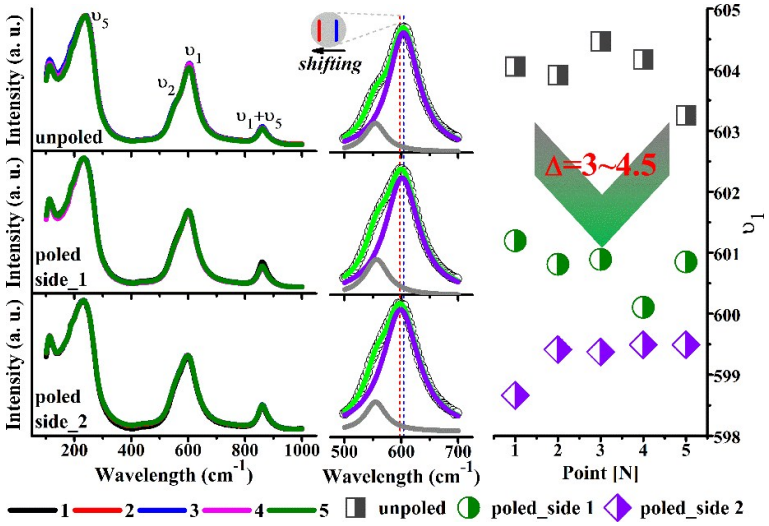

Figure S10. Raman spectra of the unpoled and poled ceramics with x=0.

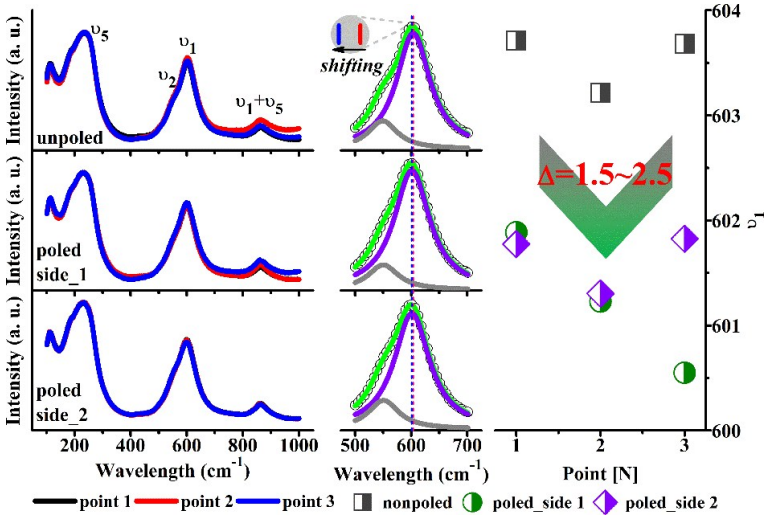

Figure S11. Raman spectra of the unpoled and poled ceramics with x=0.035.

Figure S12 shows the frequency dependence of ε_r and tan δ of the ceramics with x=0 and 0.035. The ferroelectric materials with polar nanoregions (PNRs) will exhibit the stronger dielectric relaxation than those without PNRs [15]. The dielectric relaxation will be enhanced with increasing content of PNRs [15]. Before poling, the ferroelectric domains and the PNRs exhibited the homogeneous and random distribution. Therefore, for the unpoled ceramics with x=0 and 0.035, ε_r monotonously reduce with increasing frequency, while tan δ will may increase at high frequency due to the insufficient response time for PNRs (Fig. S12). After poling, the major ferroelectric domains and the part of PNRs were rearranged along the direction of electric field, resulting in the occurrence of both "collinear" and "non-collinear" PNRs [15]. The stabilization of "collinear" PNRs will reduce the dielectric response while the destabilization of "non-collinear" PNRs will enhance the dielectric response [15]. Therefore, room-temperature ε_r and tan δ will reduce to some extent after poling. But however, such a reduction was only limited within the low frequency range due to the insufficient reorientation of PNRs [15]. The "collinear" PNRs had the enough response time at low frequency, but not enough response time at high frequency. That was the reason why the poled ceramics with x=0 and 0.035 exhibited a firstly reduced ε_r and then increased ε_r with increasing frequency, as shown in the insets in Figs. S12(a) and (b). In addition, tan δ of poled ceramics also exhibited the similar variations to those of unpoled ones (see Figs. S12(c) and (d)). Interestingly, the critical points separating two different change tendencies in frequency-dependent tan δ were changed (Figs. S12(c) and (d)). The unpoled ceramics

with x=0 exhibited no critical point in the measured frequency range, while the poled ones exhibited a critical point at 500 Hz. The unpoled ceramics with x=0.035 exhibited a critical point at 10 kHz, while the poled ones exhibited a critical point at 1 kHz. The occurrence of critical point was due to the insufficient response time for PNRs, while the reduced frequency of critical point was attributed to the "collinear" PNRs that were induced by the electric field and would fluctuate at a lower frequency than those of "non-collinear" ones.

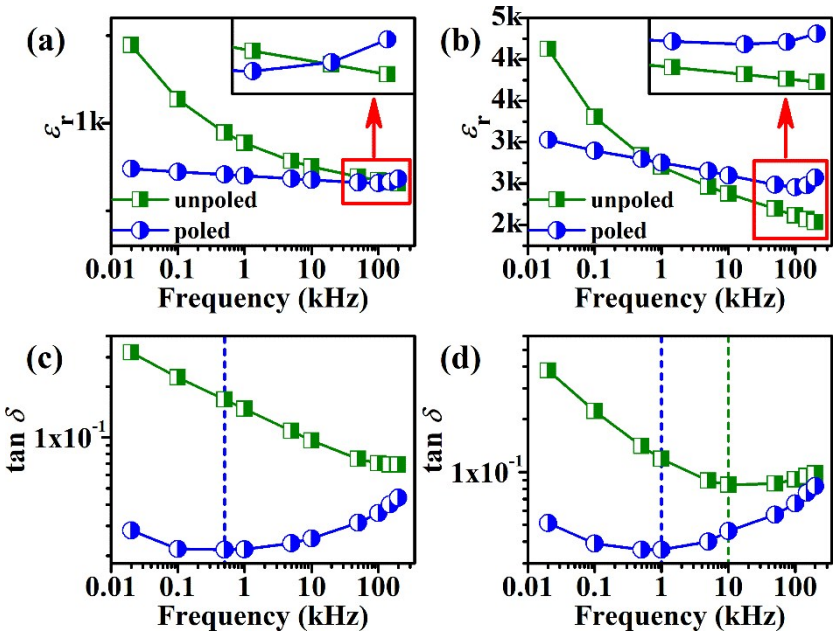

Figure S12. Frequency (20 Hz-200 kHz) dependence of ε_r and tan δ in unpoled and poled ceramics with x=0 (a, c) and x=0.035 (b, d), measured at room temperature.

Figure S13 shows the ferroelectric properties of KNNS-SZ-BAZ ceramics. The typically ferroelectric *P-E* loops were observed in the composition with x=0-0.04, indicating the decent ferroelectric properties. While the ceramics with x=0.05 exhibited a slim *P-E* loop. Fig. S13(b) shows the variations of remanent polarization (P_r), maximum polarization (P_{max}), and coercive field (E_c). P_{max} and P_r slightly reduced as x

increased from 0 to 0.035, accompanying with the relative reduction of 1.7% and 1.4%. As x exceeded 0.035, P_{max} and P_r sharply reduced. While E_c monotonously reduced with increasing x.

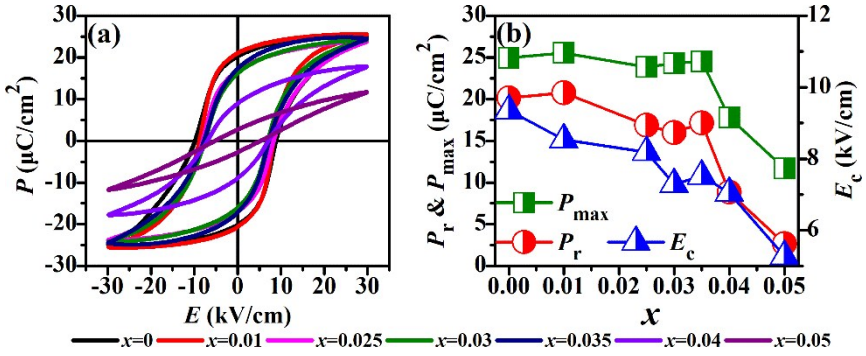

Figure S13. (a) *P*-*E* loops and (b) remanent polarization (P_r) & maximum polarization (P_{max}) & coercive field (E_c) of KNNS-SZ-BAZ ceramics.

Table S1. Electrical properties of poled KNNS-SZ-BAZ ceramics*.

x	d_{33} (pC/N)	k_p	ε_r	tan δ
0	190	0.45	617	0.0289
0.01	240	0.47	775	0.0293
0.02	320	0.52	982	0.0351
0.025	368	0.51	1191	0.0385
0.03	412	0.51	1464	0.0419
0.035	487	0.41	2486	0.0535
0.04	311	0.30	2455	0.0526
0.05	32	0	1372	0.0923

* ε_r and tan δ were measured at 100 kHz.

Table S2. Results of Rietveld refinement for the unpoled ceramic powder with x=0.035

using R+O+T combination.

	R*3*m	***Amm*2**	***P*4*mm***
Proportion	0.282	0.332	0.386
a (Å)	3.9837 (3)	3.9785 (1)	3.9771 (8)
b (Å)	3.9837 (3)	5.5578 (2)	3.9771 (8)
c (Å)	3.9837 (3)	5.7475 (6)	4.0008 (8)
α(°)	89.86	-	-
V (Å^3)	63.2207	63.5435	63.2819
A (x, y, z)	(0.0131, 0.0131, 0.0131)	(0, 0, 0.0138)	(0.0004, 0, 0.0179)
B (x, y, z)	(0.4966, 0.4966, 0.4966)	(0.4999, 0, 0.4967)	(0.4999, 0.5001, 0.4968)
O1 (x, y, z)	(0.5264, 0.5264, 0.0330)	(0, 0, 0.5328)	(0.5003, 0.5002, 0.0438)
O2 (x, y, z)		(0.4961, 0.2454, 0.2821)	(0.4999, 0, 0.5363)

Reference

1. Wu, J.; Xiao, D.; Zhu, J., Potassium-Sodium Niobate Lead-Free Piezoelectric Materials: Past, Present, and Future of Phase Boundaries. *Chem. Rev*., 2015, 115 (7), 2559-2595.

2. Wang, X.; Wu, J.; Xiao, D.; Cheng, X.; Zheng, T.; Lou, X.; Zhang, B.; Zhu, J., New Potassium-Sodium Niobate Ceramics with a Giant d_{33}. *ACS Appl. Mater. Interfaces* 2014, 6 (9), 6177-6180.

3. Zhang, Y.; Li, L.; Shen, B.; Zhai, J., Effect of orthorhombic-tetragonal phase transition on structure and piezoelectric properties of KNN-based lead-free ceramics. *Dalton Trans*., 2015, 44 (17), 7797-7802.

4. Zuo, R.; Fu, J.; Lv, D.; Liu, Y., Antimony Tuned Rhombohedral-Orthorhombic Phase Transition and Enhanced Piezoelectric Properties in Sodium Potassium Niobate. *J. Am. Ceram. Soc*., 2010, 93 (9), 2783-2787.

5. Bell, A., Phenomenologically derived electric field-temperature phase diagrams and piezoelectric coefficients for single crystal barium titanate under fields along different axes. *J. Appl. Phys*., 2001, 89 (7), 3907-3914.

6. Shannon, R. D., Revised effective ionic radii and systematic studies of interatomic distances in halides and chalcogenides. *Acta Crystallogr*., 1976, 32 (5), 751-767.

7. Zheng, T.; Wu, J.; Cheng, X.; Wang, X.; Zhang, B.; Xiao, D.; Zhu, J.; Wang, X.; Lou, X., High strain in $(K_{0.40}Na_{0.60})(Nb_{0.955}Sb_{0.045})O_3$-$Bi_{0.50}Na_{0.50}ZrO_3$ lead-free ceramics with large piezoelectricity. *J. Mater. Chem. C* 2014, 2 (41), 8796-8803.

8. Wang, D.; Hussain, F.; Khesro, A.; Feteira, A.; Tian, Y.; Zhao, Q.; Reaney, I. M., Composition and temperature dependence of structure and piezoelectricity in (1-x)(K_{1-}

$_y$Na$_y$)NbO$_3$-x(Bi$_{1/2}$Na$_{1/2}$)ZrO$_3$ lead-free ceramics. *J. Am. Ceram. Soc*., 2017, 100 (2), 627-637.

9. Wang, K.; Yao, F. Z.; Jo, W.; Gobeljic, D.; Shvartsman, V. V.; Lupascu, D. C.; Li, J. F.; Rödel, J., Temperature-Insensitive (K,Na)NbO$_3$-Based Lead-Free Piezoactuator Ceramics. *Adv. Funct. Mater*., 2013, 23 (33), 4079-4086.

10. Xu, K.; Li, J.; Lv, X.; Wu, J.; Zhang, X.; Xiao, D.; Zhu, J., Superior Piezoelectric Properties in Potassium-Sodium Niobate Lead-Free Ceramics. *Adv. Mater*., 2016, 28 (38), 8519-8523.

11. Zheng, T.; Wu, J.; Xiao, D.; Zhu, J.; Wang, X.; Xin, L.; Lou, X., Strong Piezoelectricity in (1-x)(K$_{0.4}$Na$_{0.6}$)(Nb$_{0.96}$Sb$_{0.04}$)O$_3$-xBi$_{0.5}$K$_{0.5}$Zr$_{1-y}$Sn$_y$O$_3$ Lead-Free Binary System: Identification and Role of Multiphase Coexistence. *ACS Appl Mater Interfaces* 2015, 7 (10), 5927-5937.

12. Brajesh, K.; Tanwar, K.; Abebe, M.; Ranjan, R., Relaxor ferroelectricity and electric-field-driven structural transformation in the giant lead-free piezoelectric (Ba,Ca)(Ti,Zr)O$_3$. *Phys. Rev. B* 2015, 92 (22), 224112.

13. Zhang, M.-H.; Wang, K.; Du, Y.-J.; Dai, G.; Sun, W.; Li, G.; Hu, D.; Thong, H. C.; Zhao, C.; Xi, X.-Q., High and temperature-insensitive piezoelectric strain in alkali niobate lead-free perovskite. *J. Am. Chem. Soc*., 2017, 139 (10), 3889-3895.

14. Rubio-Marcos, F.; Banares, M.; Romero, J.; Fernandez, J., Correlation between the piezoelectric properties and the structure of lead-free KNN-modified ceramics, studied by Raman Spectroscopy. *J. Raman. Spectrosc*., 2011, 42 (4), 639-643.

15. Li, F.; Zhang, S.; Yang, T.; Xu, Z.; Zhang, N.; Liu, G.; Wang, J.; Wang, J.; Cheng,

Z.; Ye, Z. G., The origin of ultrahigh piezoelectricity in relaxor-ferroelectric solid solution crystals. *Nat. Commun*., 2016, 7, 13807.